Two-dimensional manganese oxide nanolayers on Pd(100): the surface phase diagram

# Two-dimensional manganese oxide nanolayers on Pd(100): the surface phase diagram

**F Li[1], G Parteder[1], F Allegretti[1], C Franchini[2], R Podloucky[3], S Surnev[1] and F P Netzer[1]**

[1] Institute of Physics, Surface and Interface Physics, Karl-Franzens University Graz, A-8010 Graz, Austria
[2] Faculty of Physics, University of Vienna and Centre for Computational Materials Science, A-1090 Vienna, Austria
[3] Institute of Physical Chemistry, University of Vienna and Centre for Computational Materials Science, A-1090 Vienna, Austria

E-mail: francesco.allegretti@uni-graz.at and falko.netzer@uni-graz.at

**Abstract**

Two-dimensional manganese oxide layers have been grown on Pd(100) and have been characterized by means of scanning tunnelling microscopy, low energy electron diffraction and x-ray photoelectron spectroscopy (XPS). The complex surface phase diagram of $MnO_x$ on Pd(100) is reported, where nine different novel Mn oxide phases have been detected as a function of the chemical potential of oxygen $\mu_O$. Three regions of the chemical potential of oxygen can be identified, in which structurally related oxide phases are formed, often in coexistence at the surface. The different regions of $\mu_O$ are reflected in the oxidation states of the respective Mn oxide nanolayers as revealed by the Mn 2p and O 1s XPS binding energies. The $MnO_x$ nanolayers form two-dimensional wetting layers and it is speculated that they mediate the epitaxial growth of MnO on Pd(100) by providing structurally graded interfaces.

(Some figures in this article are in colour only in the electronic version)

## 1. Introduction

Manganese oxides are distinguished by a rich variety of structural, electronic and magnetic properties that have rendered them materials of interest for numerous applications. Areas of applications based on their particular physical and chemical properties, include heterogeneous catalysis, electrochemistry, environmental waste treatment, and novel electronic device technology [1–4]. As the parent compounds of the manganites, the class of complex oxides which are famous for their giant magnetoresistance effect [5], they also display a variety of interesting magnetic and electronic properties [6]. As for other transition metal oxide materials, thin films of manganese oxides supported on metal substrates bear promise for technological use and fundamental scientific studies. Thin films of MnO have been prepared with epitaxial order by various deposition methods on different noble metal

single-crystal surfaces, such as Ag(001) [7], Rh(100) [8], and Pt(111) [9, 10] surfaces. Recently, we have grown epitaxial MnO films on Pd(100) with either (100) or (111) surface orientation [11], the orientation depending on the specific kinetic parameters during growth. The epitaxial growth of MnO on all these noble metal surfaces is surprising in view of the large lattice mismatch that exists between the bulk rocksalt crystal structure of the MnO overlayer and the metallic substrates. Indeed, the lattice mismatch between Ag(001), Pt(111), and Pd(100) and MnO is ∼9%, ∼13% and ∼14%, respectively. In the present work we have set out to investigate this question of epitaxial growth in the presence of such a large lattice mismatch. We find that ultrathin layers of variable $MnO_x$ stoichiometry, only 1–2 ML thick, can be formed at the metal–MnO interface and argue that they may mediate the epitaxial growth by providing a structurally graded interface. In order to characterize these interfacial $MnO_x$ nanolayers
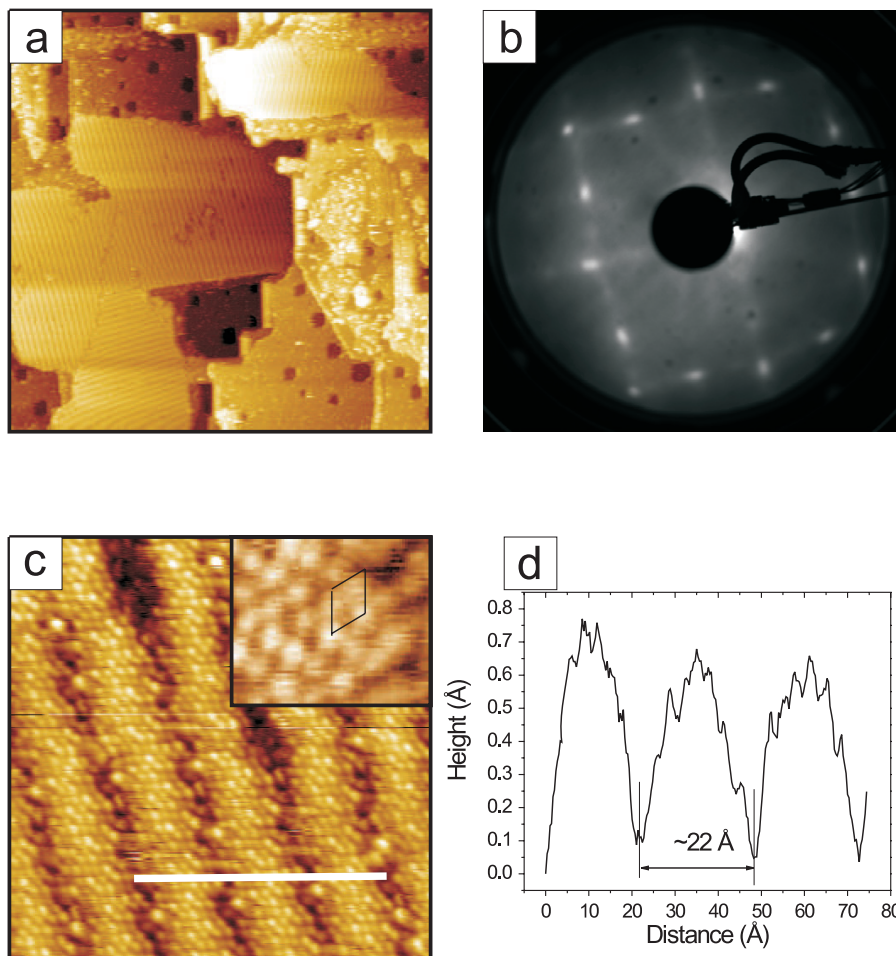
**Figure 1.** HEX-I distorted Mn oxide phase: (a) large-scale STM image (2000 Å × 2000 Å, $U = -1$ V, $I = 0.15$ nA). (b) LEED pattern ($E = 96$ eV). (c) High resolution STM images (100 Å × 100 Å, $U = +0.5$ V, $I = 0.13$ nA). Inset: (20 Å × 17 Å, $U = +0.6$ V, $I = 0.15$ nA). (d) Line profile, taken along the line indicated in panel (c).

structurally and chemically, we have transferred them from the interface to the surface and have studied the formation of two-dimensional (2D) Mn oxide monolayer structures at the surface of Pd(100) under various kinetic growth conditions.

Here, we address the multitude of different Mn oxide nanolayer phases found on Pd(100) as a function of the chemical potential of oxygen and characterize their structural properties by means of scanning tunnelling microscopy (STM) and low energy electron diffraction (LEED). The atomistic models of the major phases as derived by combining the experimental high resolution STM and vibrational electron energy loss spectroscopy (HREELS) data with *ab initio* density functional theory calculations are presented in a separate publication [12]. We find at least nine different 2D $MnO_x$ phases on Pd(100), which are novel in terms of the known Mn oxide bulk crystal structures and which are stabilized by the metal–oxide interface and the confinement in the direction perpendicular to the surface. In this paper, we introduce the manifold Mn oxide nanophases and describe an experimental phase diagram in terms of phase stability regions versus the chemical potential of oxygen, as established by means of STM, LEED and x-ray photoelectron spectroscopy.

## 2. Experimental details

STM and LEED experiments have been performed in a custom-designed ultrahigh vacuum (UHV) chamber operated at a base pressure below $2 \times 10^{-10}$ mbar, equipped with a variable-temperature atomic force–scanning tunnelling microscope (Omicron VT-AFM/STM, Germany), a four-grid LEED optics, an electron beam evaporator, a quartz crystal microbalance, and sample heating and cleaning facilities. The sample can be transferred with a magnetic transfer rod between the different preparation and analysis stages in the UHV chamber. The STM images were recorded in a constant current mode at room temperature. Electrochemically etched W tips were used, which have been cleaned *in situ* by electron bombardment.

The LEED measurements have been complemented by spot-profile analysis low energy electron diffraction (SPA-LEED) experiments performed in another UHV chamber, described in detail elsewhere [13]. High resolution x-ray photoemission measurements (HR-XPS) with use of synchrotron radiation were carried out at beamline I311 in the Swedish synchrotron radiation laboratory MAX-lab in Lund [14]. Photon energies of 620 eV and 800 eV have been
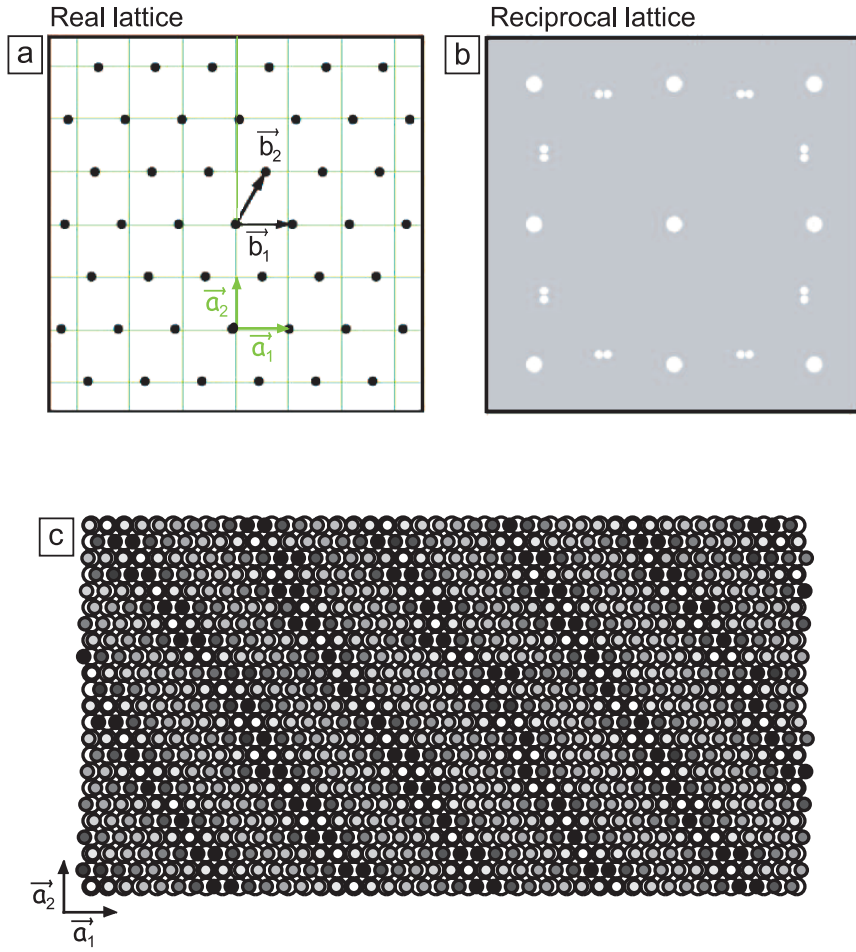
**Figure 2.** HEX-I distorted Mn oxide phase: (a) real lattice model: the square mesh corresponds to the Pd lattice with unit cell vectors ($\mathbf{a}_1$, $\mathbf{a}_2$). The black dots represent the HEX-I distorted Mn oxide lattice with unit cell vectors ($\mathbf{b}_1$, $\mathbf{b}_2$). (b) The corresponding reciprocal lattice pattern [16]. (c) A hard sphere model of the HEX-I distorted lattice superimposed on the Pd(100) lattice, reproducing the moiré pattern contrast and periodicity of the STM image in figure 1(c).

used for exciting electrons from the O 1s and Mn 2p core levels, respectively, and the corresponding experimental resolution was better than 250 meV at $h\nu = 620$ eV and 300 meV at $h\nu = 800$ eV. The core level spectra were measured at room temperature and at normal emission. The binding energy scale was calibrated with respect to the Fermi energy of the crystal in each case. The core level spectra were normalized to the secondary-electron background at a few eV lower binding energy than the respective core level peak.

Clean Pd(100) surfaces were prepared by 1.5 keV Ar$^+$-ion sputtering, followed by annealing to 1000 K for several minutes, and by heating cycles in O$_2$ atmosphere ($2 \times 10^{-7}$ mbar) at 570 K followed by a final short flash to 1000 K in UHV. Manganese oxide layers have been prepared by either reactive evaporation (RE) of Mn metal onto the clean Pd(100) surface in an oxygen atmosphere or by post-oxidation (PO) of Mn metal films. The PO procedure was found to result in more atomically smooth layers, consisting of a predominantly single oxide phase and has been therefore preferred over the RE one. Here, Mn layers were first deposited in UHV at room temperature (300 K) on the Pd(100) surface and subsequently oxidized in an oxygen atmosphere, where the oxygen pressure

was varied between $5 \times 10^{-8}$ and $5 \times 10^{-6}$ mbar and the sample temperature was between 600 and 800 K. The Mn deposition rate was monitored by a quartz crystal microbalance and typically an evaporation rate of 0.2 ML min$^{-1}$ was employed. The Mn oxide coverage is given in monolayers (ML), where 1 ML contains $1.32 \times 10^{15}$ Mn atoms cm$^{-2}$, which is equal to the Pd(100) surface density. In the present work we restrict ourselves to Mn oxide layers in the coverage region up to 1 ML.

In order to reproduce the combined effect of the temperature $T$ and the oxygen pressure $p$ on the Mn oxide surface phase diagram we plot the latter (see section 4) as a function of the chemical potential of oxygen $\mu_O(T, p)$, using the expression derived by Reuter and Scheffler [15]:

$$\mu_O(T, p) = \mu_O(T, p^o) + (1/2)kT \ln\left(\frac{p}{p^o}\right),$$

with the values of $\mu_O(T, p^o)$ tabulated in [15] at $p^o = 1$ atm.

## 3. Results and discussion

The various oxide phases discussed in the following are all characterized by specific windows in the parameter space of
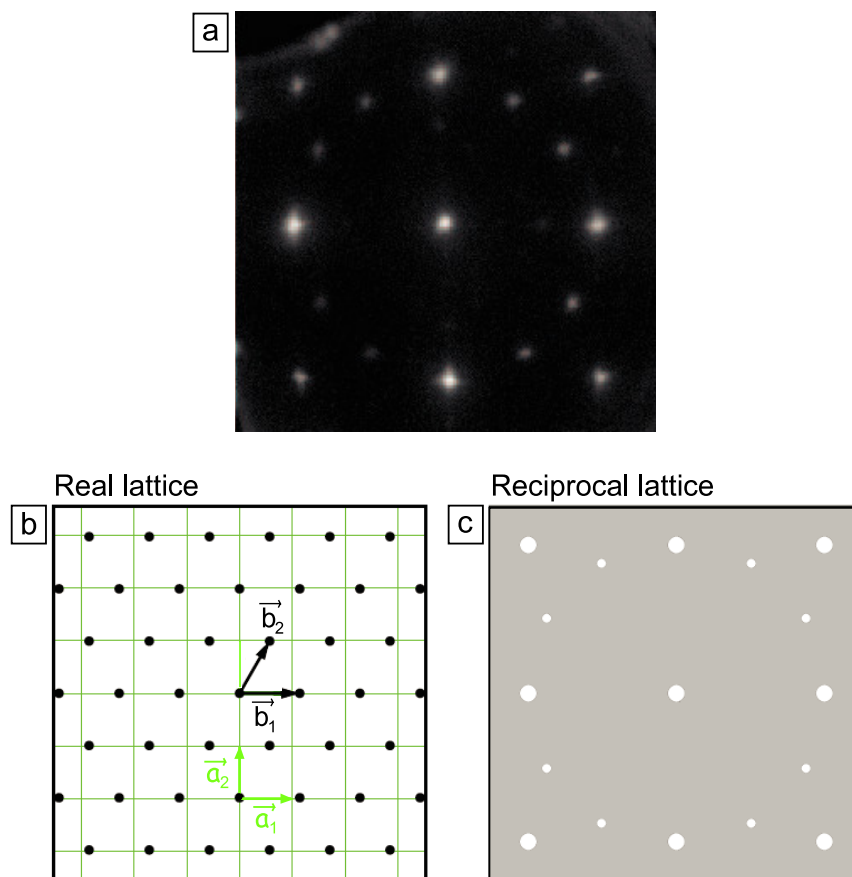
**Figure 3.** HEX-I undistorted Mn oxide phase: (a) LEED pattern ($E = 90$ eV). (b) Real lattice model: the square mesh corresponds to the Pd lattice with unit cell vectors ($\mathbf{a}_1$, $\mathbf{a}_2$). The black dots represent the HEX-I undistorted Mn oxide lattice with unit cell vectors ($\mathbf{b}_1$, $\mathbf{b}_2$). (c) The corresponding reciprocal lattice pattern [16].

the thermodynamic variables temperature and oxygen pressure. Some of the phases are stable only in a very narrow range of the parameters and this often causes the coexistence of phases that are adjacent in the phase diagram. To introduce some systematics in the presentation we will keep the oxide coverage in the range 0.75–1 ML. The sample temperature during the oxidation process has been varied in limited ranges of values: 600–700 K and 700–800 K at high and low oxygen pressure conditions, respectively. The variation of the chemical potential of oxygen during oxide formation is then mainly effected by varying the pressure of oxygen during evaporation or post-oxidation; the oxygen pressure can be converted into the chemical potential of oxygen using the standard thermodynamic expressions (see above).

*3.1. The hexagonal MnO$_x$ phases at*
*$5 \times 10^{-6}$ mbar $> p_{O_2} > 5 \times 10^{-7}$ mbar*

In this, what we call here the 'oxygen-rich', pressure regime three Mn oxide phases have been detected, which are characterized by a hexagonal or quasi-hexagonal symmetry in STM and LEED. Figure 1(a) shows a wide scan STM image of the Pd(100) surface after evaporation of Mn with an oxygen pressure in the range $5 \times 10^{-6}$–$1 \times 10^{-6}$ mbar (670 K substrate temperature). Two domains consisting of stripe structures

are recognized, which are rotated by ∼90° with respect to each other. The higher resolution STM image in figure 1(c) reveals a complicated pattern of stripes of maxima, which are separated periodically by darker troughs. The periodicity of the troughs can be measured from the line scan across the troughs (figure 1(d)) to 22–23 Å. In the high resolution STM image of the inset of figure 1(c) a quasi-hexagonal arrangement of protrusions is recognized with a lattice constant of ∼3.1 ± 0.1 Å. The LEED pattern from this surface (figure 1(b)) displays reflections close to the Pd(100) (10) and (01) substrate positions, which are elongated along the direction of the corresponding reciprocal lattice vectors, and other reflections in between the (01), (10) and (11) substrate positions that are elongated in the direction perpendicular to it: this is indicative of a quasi-hexagonal overlayer lattice. Figures 2(a) and (b) show a real space model of the overlayer (dots) on the Pd(100) lattice (grid of lines) and the corresponding simulated reciprocal space diffraction pattern [16]. Clearly, this overlayer model reflects the correct LEED pattern as experimentally observed in figure 1(b). According to this model, the overlayer lattice vectors are $\mathbf{b}_1 = 2.94$ Å and $\mathbf{b}_2 = 3.14$ Å (with angle $\theta = 60°$), and this Mn oxide phase will be designated as HEX-I *distorted*. The overlayer is incommensurate in the $\mathbf{b}_1$ direction, but in the $\mathbf{b}_2$ direction a row matching condition exists (see figure 2(a)). The STM image of figure 1(c) may
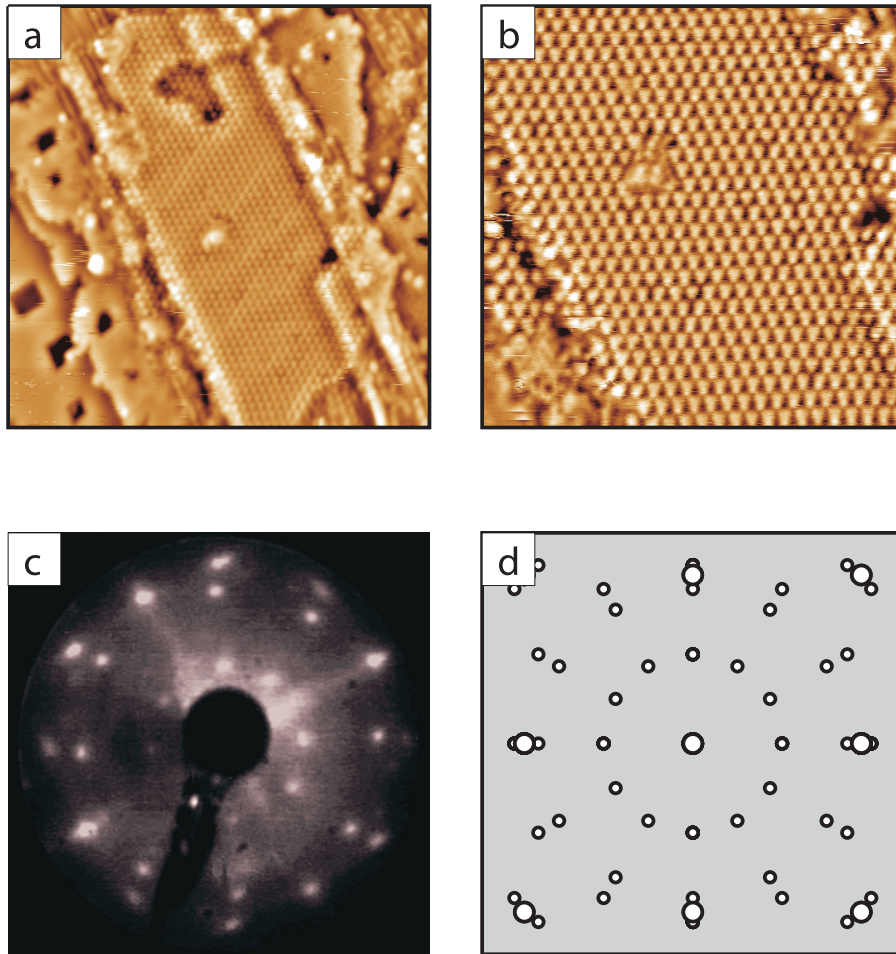
**Figure 4.** HEX-II Mn oxide structure: (a) STM image (300 Å × 300 Å, $U = +1.5$ V, $I = 0.1$ nA). (b) STM image (150 Å × 150 Å, $U = +1.5$ V, $I = 0.1$ nA). (c) LEED pattern ($E = 80$ eV). (d) Simulated LEED (reciprocal space) pattern [16].

then be understood in terms of a moiré pattern as a result of the interference of the Mn oxide overlayer lattice with the square Pd(100) surface lattice ($a_1 = a_2 = a_{Pd} = 2.75$ Å). Taking a ratio of $b_1/a_{Pd} \approx 16/15$, a moiré pattern can be constructed in a geometrical model that displays modulations in the form of broad lines inclined with respect to the Pd[110] direction ($\mathbf{a}_1$) and with an average periodicity of ∼22 Å parallel to Pd[110] (see figure 2(c)). In this model, only one type of overlayer atom is considered for simplicity, and a different colour gradation (white, grey, black) is used to highlight the different lateral registry of these overlayer atoms relative to the underlying matrix of substrate atoms. For on-top/bridge location, the white/black colour of the overlayer atoms reflects the different height above the surface. Along the $\mathbf{a}_1$ direction the same site registry is obtained for every $16 \times a_{Pd}$ lattice constants, but when including the registry along lines inclined by 60° with respect to the $\mathbf{a}_1$ direction a site registry periodicity of $8 \times a_{Pd} = 22$ Å on average is observed. The resulting modulation (figure 2(c)) is remarkably similar to the experimental STM image as seen in figure 1(c). Implicitly, this suggests an oxide film consisting of alternately stacked layers with quasi-hexagonal symmetry containing only one single atom species, as realized in the MnO(111) structure. This is discussed in detail in [12].

Under preparation conditions similar to those discussed above, another Mn oxide phase has been occasionally observed, which appears to be closely related to the *distorted* HEX-I. A LEED picture of this phase is reproduced in figure 3(a). Here, a perfectly hexagonal pattern is recognized, which corresponds to a lattice with $\mathbf{b}_1 = \mathbf{b}_2 = 3.14$ Å, and which will be referred to as *undistorted* HEX-I structure. Unfortunately, no good quality STM images have been obtained from this phase. Figures 3(b) and (c) show the real space model and the simulated diffraction pattern of the *undistorted* HEX-I [16], respectively; two orthogonal domains contribute to the pattern. The fact that the *undistorted* HEX-I is less frequently observed than the *distorted* HEX-I seems to indicate that the former structure is less stable and requires particular conditions for kinetic stabilization. We speculate that the larger lattice mismatch (14% against 7%) in the $\mathbf{b}_1$ direction and the related interfacial strain are responsible for the lower stability of the *undistorted* HEX-I as compared to the *distorted* one.

At somewhat lower oxygen pressure, in the range $1 \times 10^{-6}$ mbar $> p_{O_2} > 5 \times 10^{-7}$ mbar, a third hexagonal Mn oxide phase (HEX-II) can be observed. Figures 4(a) and (b) display STM images of this HEX-II structure, which is characterized by a hexagonal array of triangularly shaped
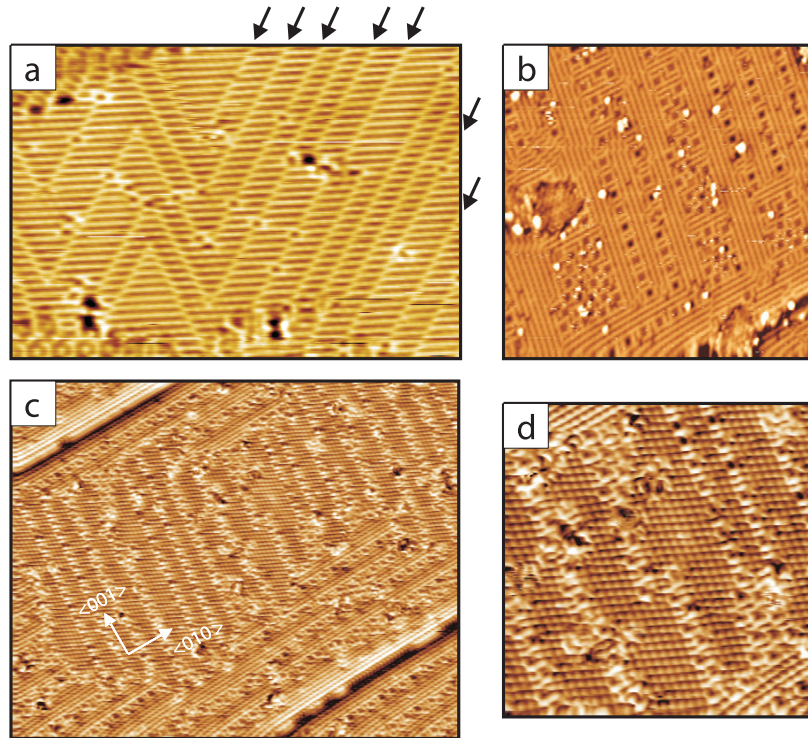
**Figure 5.** STM images of the *stripe* Mn oxide phase with anti-phase domain boundaries of two different types: (a) linear
(300 Å × 170 Å, $U = +1.4$ V, $I = 0.34$ nA) and (b) square-like (300 Å × 300 Å, $U = +0.6$ V, $I = 0.2$ nA). The arrows in (a) mark the
position of the anti-phase domain boundaries. STM images of the c(4 × 2) structure: (c) (500 Å × 500 Å, $U = +0.5$ V, $I = 0.2$ nA) and
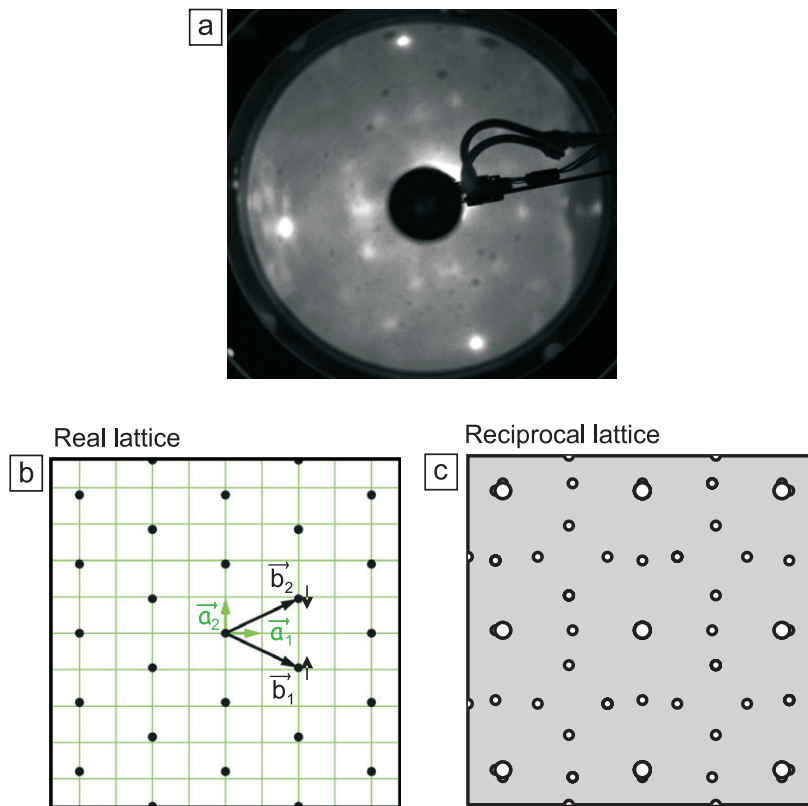(d) (200 Å × 200 Å, $U = +0.5$ V, $I = 0.2$ nA).



**Figure 6.** *Stripe* Mn oxide phase: (a) LEED pattern ($E = 60$ eV). (b) Real lattice model: the square mesh corresponds to the Pd lattice with
unit cell vectors ($\mathbf{a}_1$, $\mathbf{a}_2$). The black dots represent the *stripe* MnO$_x$ lattice with unit cell vectors ($\mathbf{b}_1$, $\mathbf{b}_2$). (c) The corresponding reciprocal
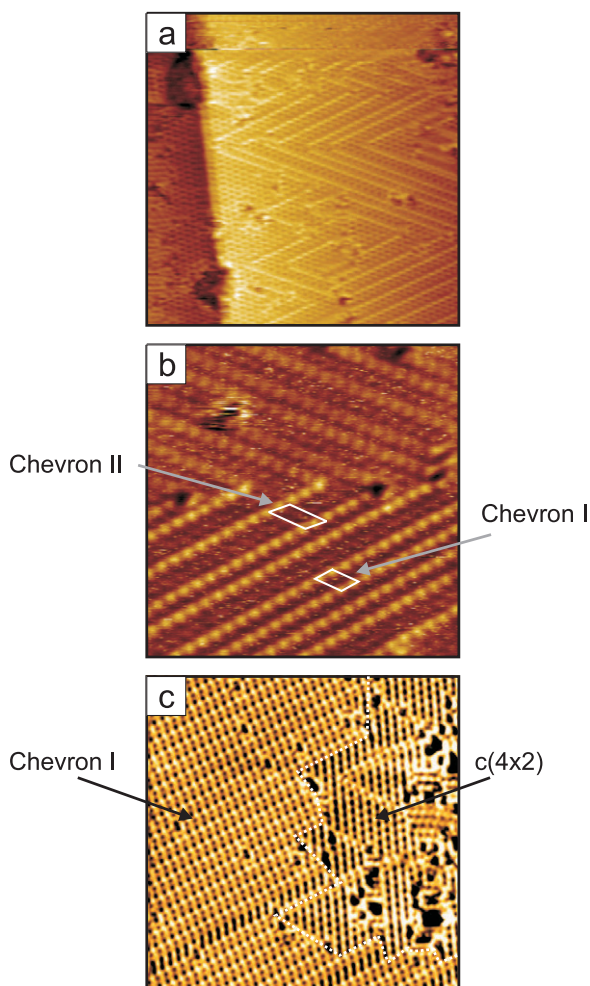lattice pattern [16].

**Figure 7.** STM images of the *chevron* Mn oxide phases:
(a) (300 Å × 300 Å, $U = +1.0$ V, $I = 0.2$ nA).
(b) (150 Å × 150 Å, $U = +1.2$ V, $I = 0.26$ nA). The unit cells of
the *chevron I* and *chevron II* structures are indicated. (c) STM image
(200 Å × 200 Å, $U = +1.0$ V, $I = 0.1$ nA) showing an area of
coexisting c($4 \times 2$) and *chevron* structures, separated by a smooth
phase boundary (white dashed line).

maxima and thus has a very different appearance in the
STM to the HEX-I phase. The HEX-II phase has the same
apparent STM height as the other two hexagonal phases. The
corresponding LEED pattern is reproduced in figure 4(c),
where the hexagonal symmetry is clearly recognized. The
lattice constant of the HEX-II oxide phase as derived from
STM and LEED is $\mathbf{b}_1 = \mathbf{b}_2 = 6.0$ Å $\pm 0.05$ Å, and the LEED
simulation in figure 4(d) confirms this lattice model.

### 3.2. The MnO$_x$ phases at 'intermediate' oxygen pressures: $5 \times 10^{-7}$ mbar $> p_{O_2} > 1 \times 10^{-7}$ mbar

At 'intermediate' oxygen pressures four different MnO$_x$ phases
have been observed. At the higher pressure end of this
regime, the so-called *stripe* phase is found at the surface
(figures 5(a) and (b)), which is often coexistent with the c($4\times2$)
structure (figures 5(c) and (d)). The *stripe* phase occurs
with two different appearances, which are caused by different
arrangements of anti-phase domain boundaries. In figure 5(a)

bands of parallel stripes are formed by the domain boundaries
running at an angle of 60° with respect to the stripes (see the
arrows on the figure); this results in w-shaped structure motifs.
In figure 5(b) the anti-phase domain lines run in orthogonal
directions, resulting in small square or rectangular domains.
The separation between the stripes is ∼5.5 Å, which is $2 \times a_{Pd}$,
while along the stripes maxima separated by ∼5.4 Å have
been recognized in some STM images. The *stripe* phase thus
appears to be a quasi-hexagonal phase; this is supported by the
analysis of the LEED pattern, which is discussed below.

The c($4 \times 2$) structure is the central oxide phase in this
pressure regime. It is a commensurate structure, characterized
by $\mathbf{b}_{1,2} = 6.15$ Å or by the transformation matrix $\mathbf{M} =$
[2, −1/2, 1]. Under carefully controlled kinetic conditions the
c($4 \times 2$) structure forms a single-phase wetting layer as shown
in the STM images of figures 5(c) and (d). In figure 5(c),
well-ordered c($4\times 2$) domains, in two orthogonal directions,
are separated by disordered phase boundaries. The latter
presumably act to relieve interfacial strain. The c($4 \times 2$) MnO$_x$
structure observed here is similar to the c($4 \times 2$) Ni oxide
monolayer structure on Pd(100) as reported by Agnoli *et al*
[17]. The latter has been interpreted in terms of a compressed
NiO-type monolayer with a c($4 \times 2$) Ni vacancy array, yielding
an overall stoichiometry of Ni$_3$O$_4$. We suggest that a similar
model may also be applicable in the case of c($4\times2$) MnO$_x$ [12].

The LEED pattern displayed in figure 6(a) is from a
surface, which contained mainly the *stripe* oxide phase; due
to limited long-range order the pattern is diffuse, but the
relevant features can still be recognized. We argue that
the *stripe* structure can be created by a distortion of the
c($4 \times 2$) lattice. Figure 6(b) illustrates this point: by a
uniaxial compression of the c($4 \times 2$) unit cell of 5% along
the $\mathbf{a}_2$ direction (arrows in figure 6(b)) a transformation matrix
of $\mathbf{M} = $ [2, −0.95/2, +0.95] is obtained. The structure
according to this transformation matrix yields the diffraction
pattern of figure 6(c) [16], which reproduces remarkably well
the experimental LEED pattern of figure 6(a).

At the lower pressure end of the 'intermediate' pressure
regime the c($4 \times 2$) phase is often observed in coexistence with
the so-called *chevron* structures (figure 7). The name for these
structures has been deduced from the 'chevron-like' structure
motifs as seen in figure 7(a), which are derived from different
domains separated by anti-phase domain boundaries. There
are two structures, *chevron I* and *chevron II,* corresponding
to the transformation matrices $\mathbf{M} = $ [2, −1/3, 2] and $\mathbf{M} = $
[2, −1/5, 3], respectively. In STM, these structures consist
of rows of maxima (figure 7(b)), with unit cell vectors $\mathbf{b}_1 =$
6.15 Å, specifying the common distance of maxima along
the rows, and $\mathbf{b}_2 = 9.92$ Å and 16.04 Å for *chevron I*
and *II*, respectively; the latter define the distances between
the rows. The unit cells for the two structures *I* and *II*
are indicated on figure 7(b). The phase boundaries between
the two *chevron* structures and the c($4 \times 2$) structure are
smooth and continuous (see the dashed line in figure 7(c)),
suggesting that these phases are structurally closely related.
This is also supported by the observation that there is no height
difference in STM between the various structures. Indeed,
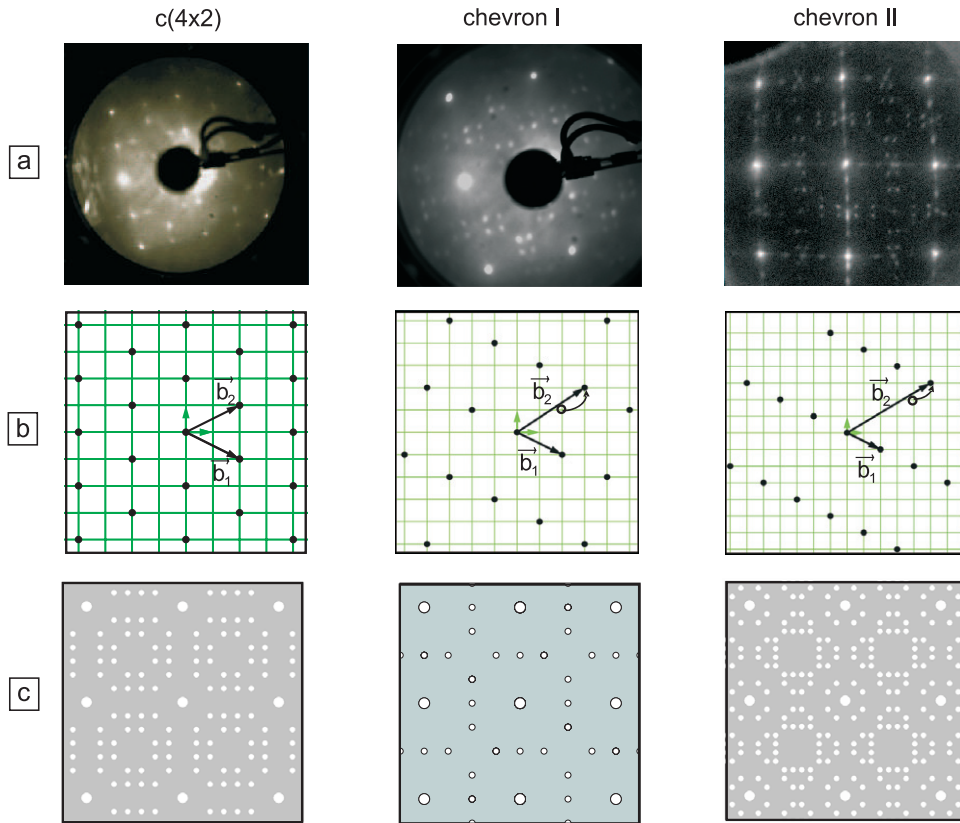the unit cells of the *chevron* structures can be generated from

**Figure 8.** LEED patterns (a), real lattice models (b) and reciprocal lattice patterns (c) of the c(4 × 2) (left panel), *chevron I* (middle panel) and *chevron II* (right panel) structures. The respective LEED energies in (a) are 116, 108 and 60 eV.

the c(4 × 2) structure by a simple extension of the $\mathbf{b}_2$ unit cell vectors to adjacent anti-phase positions as illustrated in figure 8(b). Figure 8(a) displays the experimentally observed LEED patterns of the c(4 × 2), *chevron I* and *II* structures, whereas figure 8(c) shows the computer simulated patterns derived from the structure models of figure 8(b) [16]. There is excellent agreement between the experimental and simulated patterns. The formation of the *chevrons* from the c(4 × 2) structure can be rationalized in terms of a Mn vacancy propagation model as discussed in [12].

### 3.3. The MnO$_x$ phases in the 'oxygen-poor' regime: $1 \times 10^{-7}$ mbar > $p_{O_2}$ > $5 \times 10^{-8}$ mbar

There is a smooth transition from the c(4 × 2) and *chevron* structures of the intermediate oxygen pressure regime to the structures in the 'oxygen-poor' regime: *labyrinth* and *waves*, which are named according to their STM pattern. In the STM image of figure 9(a) three large terraces are seen, where the upper left and the lower right terraces are covered by the *labyrinth* (L) structure, whereas the middle terrace is coated by the *waves* (W). The lines that run parallel to the step edges belong to the c(4 × 2) structure. Figure 9(c) shows a close-up of the *labyrinth* structure; at the step edge the c(4 × 2) structure is clearly recognized here. The *labyrinth* structure is described using the lattice vectors $\mathbf{b}_1 = 13.5 \pm 0.5$ Å and $\mathbf{b}_2 = 11.0 \pm 0.5$ Å, $\theta = 85° \pm 2°$, the unit cell is rotated by $\alpha = 21° \pm 2°$ with respect to the Pd[011] direction. The *waves*

structure is illustrated in the STM images of figure 9(b) and in the LEED pattern of figure 9(d). The unit cell is characterized by $\mathbf{b}_1 = 13.8 \pm 0.2$ Å, $\mathbf{b}_2 = 34 \pm 1$ Å, $\theta = 90° \pm 2°$, which corresponds approximately to a (5 × 12) superstructure with respect to the Pd(100) substrate. This is compatible with the LEED pattern of figure 9(d). From the STM images, the periodicity along the $\mathbf{b}_2$ direction may also be twice as large, supporting a (5 × 24) superstructure. The *labyrinth* and *waves* structures are characterized by the same apparent height in STM.

In figure 9(b) an embedded island is visible in the centre, where a different structure can be perceived. This structure with a hexagonal symmetry is formed best at the low oxygen pressure end of this regime or by the oxidation of Mn atoms that have segregated from the Pd substrate bulk to the surface (after prolonged use of the Pd crystal as a substrate for Mn oxide growth, some Mn atoms become dissolved in the Pd bulk). This HEX-III structure is shown more clearly in the STM image of figure 10(a), with the corresponding LEED pattern in figure 10(b). The HEX-III structure is described using the transformation matrix $\mathbf{M} = [0, 2/\sqrt{3}, 1]$ with respect to Pd(100), but corresponds also to a $(\sqrt{3} \times \sqrt{3})$R30° superstructure with respect to a MnO(111) surface. It is possible that this structure is an interfacial phase that mediates the growth of MnO(111) oriented films, which has been reported previously [11].
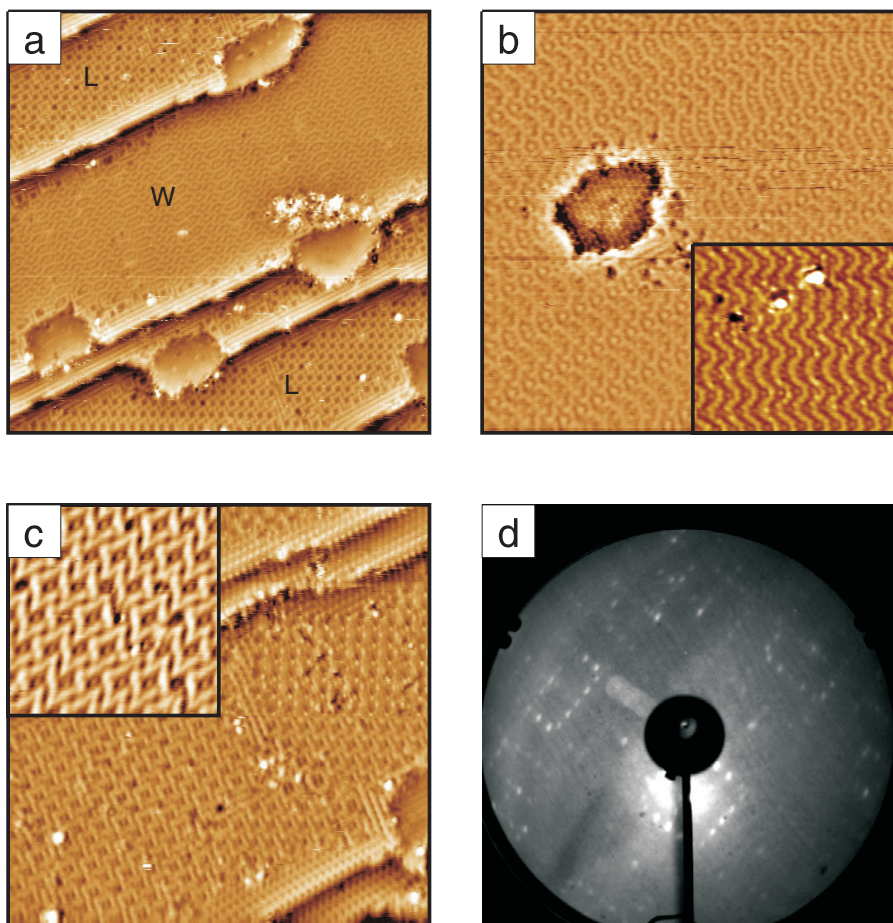
**Figure 9.** (a) STM image (500 Å × 500 Å, $U = +1.5$ V, $I = 0.1$ nA) of *labyrinth* (L) and *waves* (W) Mn oxide structures covering neighbouring terraces on the Pd(100) surface. (b) High resolution STM images of the *waves* structure (300 Å × 300 Å, $U = +0.6$ V, $I = 0.3$ nA). Inset: (200 Å × 200 Å, $U = +1.4$ V, $I = 0.3$ nA). (c) High resolution STM images of the *labyrinth* structure (300 Å × 300 Å, $U = +0.6$ V, $I = 0.3$ nA). The terrace areas close to the step edges are covered by the c(4× 2) phase. Inset: (90 Å × 90 Å, $U = +0.1$ V, $I = 0.45$ nA). (d) LEED pattern of the *waves* structure (100 eV).

### 3.4. Mn 2p and O 1s XPS core level spectra

In figure 11(a) we show two representative Mn $2p_{3/2}$ XPS core level spectra of the HEX-I and the *waves* phases. The Mn 2p core level photoemission lines of Mn oxides are broad and display a complex shape due to multiplet splitting, correlation and configuration interaction effects in the final state [18]. Moreover, in oxide nanolayers on metals the screening from the substrate influences the determination of the cation oxidation state by comparison with bulk oxide XPS data. Thus, the absolute Mn $2p_{3/2}$ binding energies measured in figure 11(a) at around 640–641.5 eV, i.e. at values typical for MnO, are perhaps not too meaningful. However, the shift of the Mn 2p binding energy of 0.8 eV between the HEX-I and the *waves* structure is significant and justifies the separation of the MnO$_x$ phase diagram into an 'oxygen-rich' region with phases of higher oxidation state and an 'oxygen-poor' region with lower oxidation state Mn oxides. Direct confirmation of this conclusion is provided by the O 1s spectra reported in figure 11(b). Here, the O 1s core level intensity is strongly reduced when moving from the HEX-I to the *waves* phase. Although photoelectron diffraction may contribute to this effect, its contribution is typically much smaller than the

intensity reduction observed in figure 11(b). The experimental evidence therefore suggests markedly different stoichiometries for the 'oxygen-rich' and 'oxygen-poor' regions. Interestingly, the broad O 1s line-shape for the HEX-I phase points to the presence of two oxygen components, one centred at 529.1 eV and the other chemically shifted to higher binding energy by roughly 0.4 eV. This is indicative of an oxide layer with differently coordinated O ions, as confirmed by the structural model presented in [12].

### 4. Conclusions

The formation of two-dimensional MnO$_x$ nanolayer phases on Pd(100) has been studied by means of STM, LEED and XPS as a function of the oxygen pressure during preparation at a substrate temperature of ∼700 K. The complex phase diagram of 2D Mn oxide structures on Pd(100) as displayed in figure 12 in the form of the stability region of oxide phases versus the chemical potential of oxygen $\mu_O$ summarizes the results of this investigation. Nine major 2D oxide nanophases have been detected in the accessible region of the parameter space. In the so-called 'oxygen-rich' region, at $\mu_O = -1.15$–$1.35$ eV,

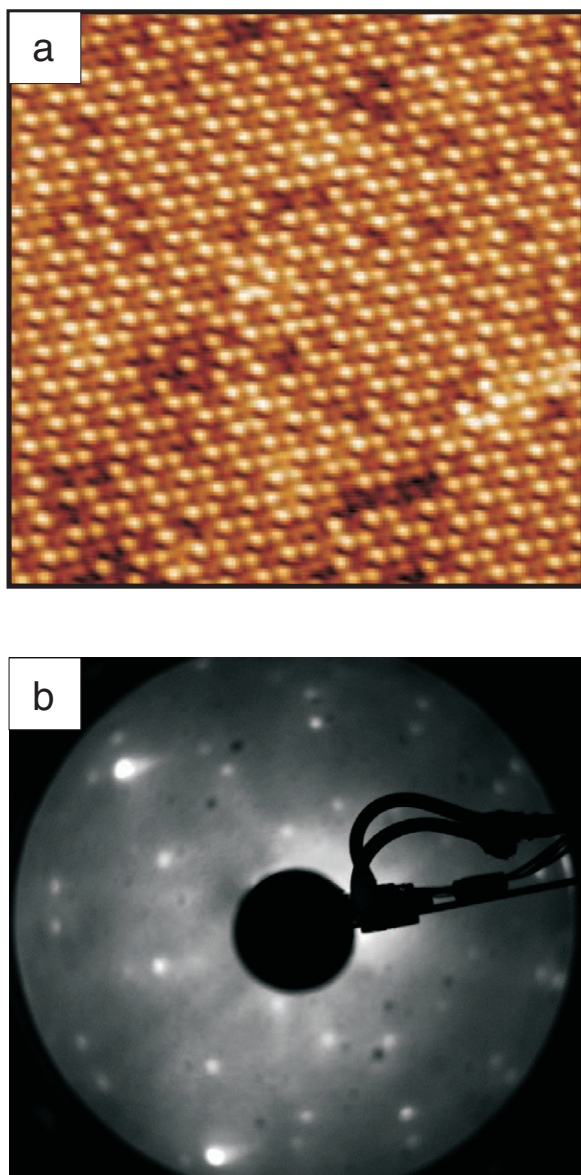**Figure 10.** (a) STM image (90 Å × 90 Å, $U = +3.3$ mV, $I = 1.0$ nA) and (b) LEED pattern (85 eV) of the HEX–III Mn oxide phase.



**Figure 11.** (a) Mn 2p$_{3/2}$ and (b) O 1s core level spectra of the HEX–I (top curves) and *waves* (bottom curves) Mn oxide phases.

the hexagonal phases HEX-I and HEX-II have been observed, the former in two modifications as *distorted* and *undistorted* hexagonal structures. At 'intermediate' chemical potentials, $\mu_O = -1.35$–$1.45$ eV corresponding roughly to the $10^{-7}$ mbar oxygen pressure region, the c(4 × 2) MnO$_x$ structure is the central phase. The other structures found in this region are the *stripe,* the *chevron I* and the *chevron II* structures. The latter overlayers are closely related to the c(4 × 2) phase as indicated by their frequent coexistence at the surface and the smooth boundary regions between them. At 'low' chemical potentials of oxygen, $\mu_O < -1.45$ eV, the *waves* and *labyrinth* structures are observed, which have complex unit cells and for which the connection to the phases at intermediate oxygen potentials is less clear. At the lowest $\mu_O$, an additional hexagonal phase HEX-III is formed with unit cell dimensions that are related to those of the MnO(111) face. Although the nominal Mn
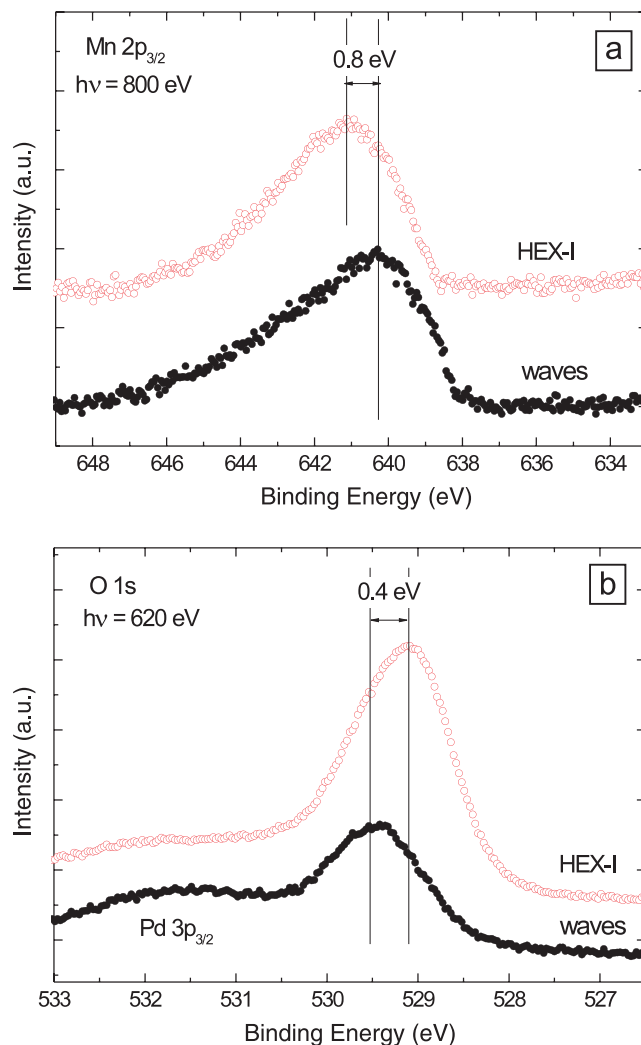
coverages are between 0.75 and 1 ML for all phases, the actual oxide coverages depend on the specific oxide structure: they vary therefore somewhat in the different regimes. The oxide phases in the 'oxygen-rich' regime have higher apparent STM heights than those of the 'intermediate' and 'oxygen-poor' regimes. However, within each regime, the apparent heights of the phases are very similar. Finally, we mention that the MnO$_x$ phases described above are the ones which have been reproducibly observed many times. There are several intermediate phases which have been seen only occasionally and which seem to be metastable and only stabilized under particular kinetic conditions.
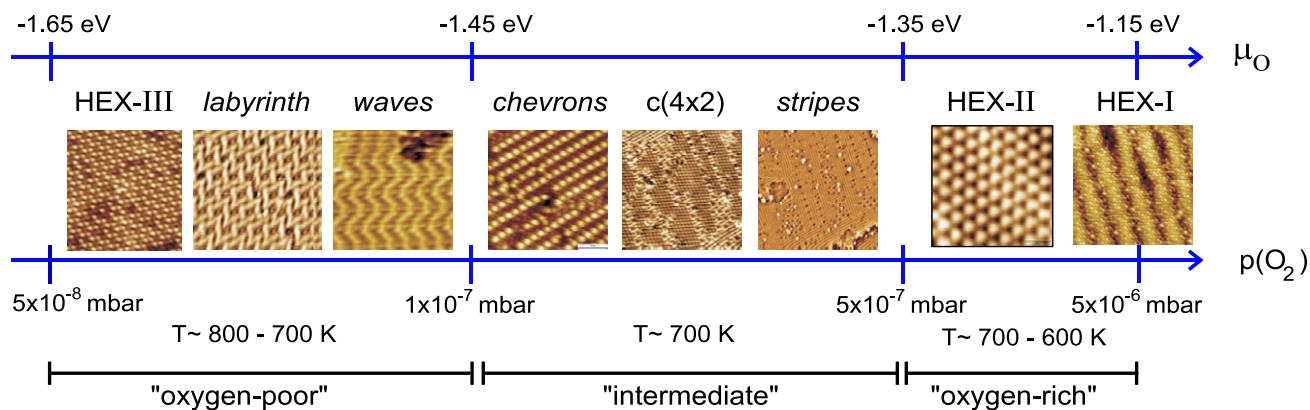
## Acknowledgments

**Figure 12.** Schematic phase diagram of the 2D Mn oxides, presented as a function of the oxygen pressure $p(O_2)$ and of the oxygen chemical potential $\mu_O$. The nominal coverage of Mn on Pd(100) is 0.75 ML.

# References

[1] Baldi M, Finocchio E, Pistarino C and Busca G 1998 *Appl. Catal.* A **173** 61

[2] Armstrong A R and Bruce P G 1996 *Nature* **381** 499

[3] Taillefert M, MacGregor B J, Gaillard J F, Lienemann C P, Perret D and Stahl D A 2002 *Environ. Sci. Technol.* **36** 468

[4] Han M J, Ozaki T and Yu J J 2005 *J. Chem. Phys.* **123** 034306

[5] Von Helmholtz R, Wecker J, Holzapfel B, Schultz L and Samwer K 1993 *Phys. Rev. Lett.* **71** 2331

[6] Pask J E, Singh D J, Mazin I I, Hellberg C S and Kortus J 2001 *Phys. Rev.* B **64** 024403

[7] Müller F, De Masi R, Reinicke D, Steiner P, Hüfner S and Stowe K 2002 *Surf. Sci.* **520** 158

[8] Nishimura H, Tashiro T, Fujitani T and Nakamura J 2000 *J. Vac. Sci. Technol.* A **18** 1460

[9] Rizzi G A, Zanoni R, Di Siro S, Perriello L and Granozzi G 2000 *Surf. Sci.* **462** 187

[10] Hagendorf Ch, Sachert S, Bochmann B, Kostov K and Widdra W 2008 *Phys. Rev.* B **77** 075406

[11] Allegretti F, Franchini C, Bayer V, Leitner M, Parteder G, Xu B, Fleming A, Ramsey M G, Podloucky R, Surnev S and Netzer F P 2007 *Phys. Rev.* B **75** 224120

[12] Franchini C, Podloucky R, Allegretti F, Li F, Parteder G, Surnev S and Netzer F P 2009 *Phys. Rev.* B **79** 035420

[13] Schoiswohl J, Zheng W, Surnev S, Ramsey M G, Granozzi G, Agnoli S and Netzer F P 2006 *Surf. Sci.* **600** 1099

[14] Nyholm R, Andersen J N, Johansson U, Jensen B N and Lindau I 2001 *Nucl. Instrum. Methods Phys. Res.* A **467/468** 520

[15] Reuter K and Scheffler M 2001 *Phys. Rev.* B **65** 035406

[16] LEED simulation software http://w3.rz-berlin.mpg.de/~hermann/LEEDpat/

[17] Agnoli S, Sambi M, Granozzi G, Schoiswohl J, Surnev S, Netzer F P, Ferrero M, Ferrari A M and Pisani C 2005 *J. Phys. Chem.* B **109** 17197

[18] van Elp J, Potze R H, Eskes H, Berger R and Sawatzky G A 1991 *Phys. Rev.* B **44** 1530